A comprehensive control system for multi-parallel grid-connected inverters with LCL filter in weak grid condition

Akhavan, Ali; Mohammadi, Hamid Reza; Guerrero, Josep M.

A Comprehensive Control System for Multi-Parallel Grid-Connected Inverters with *LCL* Filter in Weak Grid Condition

Ali Akhavan, Hamid Reza Mohammadi, and Josep M. Guerrero

Abstract: Active damping methods are used for resonance damping in grid-connected inverters with *LCL* filter. In microgrids, parallel grid-connected inverters are coupled due to grid impedance introducing multiple resonances. In general, such coupling effect is not taken into account for modeling and controller design. For single grid-connected inverter, despite good performance, the system tends to become instable with parallel connection of other inverters. Moreover, the grid injected current can be distorted by the grid voltage harmonics. In traditional control system, grid voltage is used as a feedforward signal to achieve harmonic rejection capability by boosting the inverter output impedance. However, this method introduces negative phase angle which could lead to control system instability. In this paper, the control system design for multi-parallel grid-connected inverters using active damping is clarified. Inverters with different characteristics are also modeled in a weak grid as a multivariable system while coupling effect with a wide variation of grid impedance is taken into account. An improved grid voltage feedforward method is proposed to eliminate negative aspects of the traditional method. The simulation results in MATLAB/SIMULINK software demonstrate the effectiveness of the proposed control system.

Keywords: Multi-parallel inverters, Active damping, Coupling effect, Grid voltage feedforward method, *LCL* filter

1. Introduction

Grid-connected inverters are essential elements in converting nearly all kinds of generated power in distributed generation plants into a high quality AC power to be injected reliably into the grid [1]. The quality of grid injected current in grid-connected systems is a matter of concern [2]. Thus, a low-pass filter is used to filter out the switching frequency harmonics of the inverter output current. The *LCL* filter is preferred in comparison with other low-pass filters such as *L* and *LC* because of better switching harmonic attenuation and reduced filter size at the same time [3], [4]. Nevertheless, due to resonance of the *LCL* filter, a damping method is needed to stabilize the system [5]. Resonance damping methods for *LCL* filters, including passive and active damping methods have been extensively discussed in literatures [6-9]. Power loss in passive damping methods is the biggest drawback. Hence, active damping is preferred over passive mainly damping due to its high efficiency and flexibility. Dual-loop active damping methods are widely used for resonance damping. These methods are based on feedback of the state variables of *LCL* filter such as capacitor current [1], [10-13], capacitor voltage [14], grid-side inductor current [15], [16] and inverter-side inductor current [17].

A main challenge is encountered when multi-parallel grid-connected inverters are coupled through grid impedance Z_g. In Fig. 1, the voltage of Point of Common Coupling (PCC), V_{pcc}, is shared by all inverters and can be modified by their injected currents [18]. Therefore, all inverters influence each other due to grid impedance existence. Depending on the number of parallel inverters and grid impedance value, the inverters installed in a microgrid may not behave as expected. It is worth nothing that, multi-parallel grid-connected inverters also introduce

multiple resonances whose frequency and peak can be varied with variations of the grid impedance and number of inverters [19].

Furthermore, grid voltage in weak grids usually contains harmonic components which are created by non-linear loads connection at other buses. The grid voltage harmonics can therefore greatly distort the grid-injected current. Hence, the inverter control system should be designed with harmonic rejection capability which is closely correlated with the inverter output impedance [10]. Recently, a popular approach attracting attention is employing the grid voltage feedforward method in the control system to enhance the inverter output impedance [5].
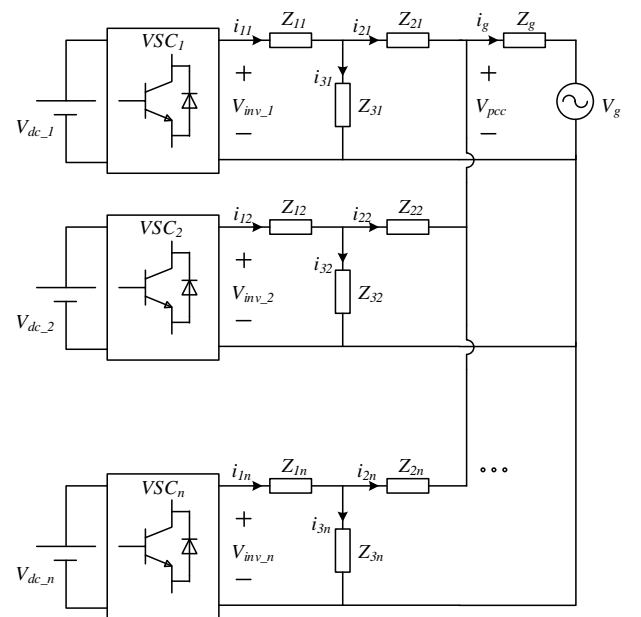

Fig. 1. Typical multi-parallel grid-connected inverters.

1

Although this method can boost considerably the inverter output impedance, it nevertheless introduces negative phase angle to the control system which could lead to instability in weak grids [1].

Many literatures regarding active damping strategies are published for single grid-connected inverter systems [10-17], [20-23]. However, the coupling effect among inverters due to grid impedance is not considered. In [24], an optimal virtual flux predictive direct power control (VF-PDPC) is proposed for a three-phase grid-connected inverter which operating under unbalanced and distorted grid voltage. Despite good performance of the control system, only one inverter is considered and coupling effect among inverters in a microgrid containing several inverters is not addressed. In [18], a PV power plant contains N parallel grid-connected inverters has been modeled as a multivariable system. However, all inverters are assumed to be the same. In [25], the inverters with different characteristics in a microgrid are modeled as a multivariable system and controller design process is introduced praiseworthy, but the effect of grid voltage harmonics on the grid injected current is not considered. Multiple resonances in a microgrid are investigated in [19]. However, the control system design is done without considering the coupling effect among inverters.

In this paper, modeling and control of three parallel single-phase grid-connected inverters in a weak grid condition is described. In the proposed scheme, the wide variation of grid impedance and also grid voltage harmonics are considered. Unlike [18], all inverters may have different characteristics. Also, dual-loop active damping control using capacitor current feedback is chosen for its simple and effective implementation. A simple but effective improved grid voltage feedforward method is proposed which suppress the effect of grid voltage harmonics by boosting the inverter output impedance, while eliminates the negative aspect of traditional method such as introducing negative phase angle to the control system in weak grids. Then, the system stability is investigated based on impedance-based stability criterion [26]. The deficiencies of traditional grid voltage feedforward method are:

1. Introducing a negative phase angle to close loop control system. Consequently, the phase margin is reduced and it may be causes the system instability.
2. Ignoring the coupling effect between inverters. Consequently, the overall system maybe unstable whereas the connection of each individual inverter is stable.

The suggestions in the proposed comprehensive control system are:

1. Using a proportional gain in an improved grid voltage feedforward method which mitigates the first deficiency.
2. Precise modeling and controller design for multi-parallel grid-connected inverters (with different parameters) considering the coupling effect between inverters. In this way, the second deficiency is mitigated.

This paper is organized as follows. In Section 2, modeling and control of a single grid-connected inverter is described. Norton equivalent circuit and the proposed grid voltage feedforward method are presented in this section. In Section 3, modeling and control of three parallel grid-connected inverters with different characteristics are described. In Section 4, controller design process for the multivariable control system that is modeled in section 3 is described. In Section 5, the theoretical study is validated through numerous simulations in MATLAB/Simulink software. Finally, Section 6 concludes the paper.

2. Control of a Single Grid-Connected Inverter in a Weak Grid

In this section, the modeling and control of a single grid-connected inverter is described. Then, a simple but effective improved grid voltage feedforward method is proposed.

2.1. Modeling of a Single Grid-Connected Inverter

Fig. 2 shows the general structure of an *LCL*-filtered grid-connected inverter. The *LCL* filter consists of an inverter-side inductor L_1, a grid-side inductor L_2, and a filter capacitor C.

$$Z_1 = L_1.s, \ Z_2 = L_2.s, \ Z_3 = \frac{1}{C_3.s}, \ Z_g = L_g.s \qquad (1)$$

In this figure, V_{dc} is the input DC voltage, V_{inv} is the output voltage of the inverter bridge, i_1, i_g, and i_C are inverter-side current, grid-side current and capacitor current, respectively. Also, $G_i(s)$ is the current regulator and i_C is fed back to damp the *LCL* filter resonance. At the PCC, the grid is modeled by its Thevenin equivalent circuit for simplicity, consisting of a voltage source V_g in series with grid impedance Z_g. $G_d(s)$ is the transfer function which combines the computational and PWM delays [18].

$$G_d(s) = \frac{1 - 0.5.s.T_s}{(1 + 0.5.s.T_s)^2} \qquad (2)$$

where, T_s refers to sampling period.

With the aforementioned model, the linearized model of a single grid-connected inverter with *LCL* filter in *s*-domain can be derived as shown in Fig. 3(a). In this figure, K_{P_inner} is the proportional controller in the inner loop. Considering Fig. 3(a), adequate controller design is quite complicated due to interacting loops. In order to simplify the design procedure, an equivalent model with decoupled regulating loops would be desirable. The model in Fig. 3(a) can be simplified by adding capacitor voltage (v_C) to output signal of the transfer function K_{P_inner}, and by replacing feedback signal i_C with i_1-i_g as shown in Fig. 3(b).

Using the equivalent transformations presented in [1] and [10], the block diagram of Fig. 3(a) can be transformed into Fig. 4. $G_{x1}(s)$ and $G_{x2}(s)$ transfer functions are given by
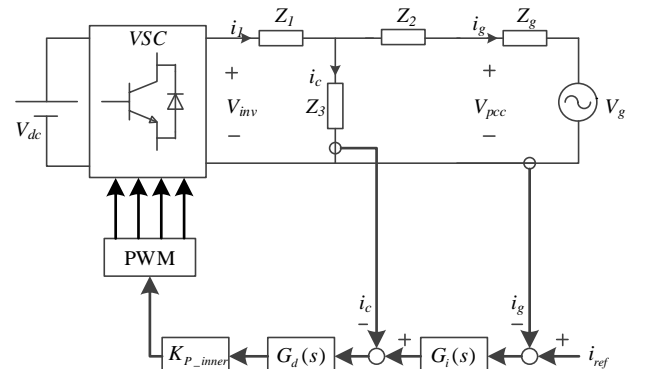

Fig. 2. Configuration of a single grid-connected inverter with *LCL* filter.

$$G_{x1}(s) = \frac{K_{P\_inner}G_d(s)}{s^2 L_1 C + sCK_{P\_inner}G_d(s)+1} \cdot G_i(s) \qquad (3)$$

$$G_{x2}(s) = \frac{s^2 L_1 C + sCK_{P\_inner}G_d(s)+1}{s^3 L_1 L_2 C + s^2 L_2 CK_{P\_inner}G_d(s) + s(L_1 + L_2)} \qquad (4)$$

Hence, according to Fig. 4, the current loop gain $T(s)$ can be derived as

$$T(s) = G_{x1}(s)G_{x2}(s)$$

$$= \frac{K_{P\_inner}G_d(s)G_i(s)}{s^3 L_1 L_2 C + s^2 L_2 CK_{P\_inner}G_d(s) + s(L_1 + L_2)} \qquad (5)$$

As shown in Fig. 5, a grid-connected inverter can be modeled by its Norton equivalent circuit, consisting of an ideal current source $i_s(s)$ in parallel with an admittance $Y_o(s)$.

In Fig. 5, the grid is modeled by its Thevenin equivalent circuit consisting of an ideal voltage source $V_g(s)$ in series with the grid impedance $Z_g(s)$. According to this figure, the injected grid current $i_g(s)$ can be obtained as

$$i_g(s) = i_s(s) - \frac{v_{pcc}(s)}{Z_o(s)} ; \quad Y_o(s) = \frac{1}{Z_o(s)} \qquad (6)$$

The Norton equivalent current source ($i_s(s)$) which is equal to short circuit current at PCC ($V_{pcc}=0$), can be obtained using Fig. 4 as

$$i_s(s) = \frac{T(s)}{1+T(s)} \cdot i_{ref}(s) = G_{cl} \cdot i_{ref}(s) \qquad (7)$$

where G_{cl} is closed-loop transfer function of control system. Also, $Z_o(s)$ is equal to inverter output impedance, which can be obtained using Fig.4 as

$$Z_o(s) = \left.\frac{v_{pcc}}{-i_g(s)}\right|_{i_s(s)=0} = \frac{1+T(s)}{G_{x2}(s)} \qquad (8)$$

Using superposition theorem in Fig. 5, the injected grid current $i_g(s)$ can be obtained as (9).

$$i_g(s) = \frac{Z_o(s)}{Z_o(s) + Z_g(s)} i_s(s) - \frac{1}{Z_o(s) + Z_g(s)} V_g(s) \qquad (9)$$

Referring to (9), in order to suppress the grid current distortion caused by $V_g(s)$, the magnitude of $Z_o(s) + Z_g(s)$ should be as high as possible.

2.2. Grid Voltage Feedforward Method

As demonstrated in previous subsection, the grid voltage harmonic rejection capability of a grid-connected inverter can be achieved by increasing the magnitude of $Z_o(s)$ + $Z_g(s)$. Since $Z_g(s)$ is determined by power grid, only $Z_o(s)$ can be shaped to achieve the high magnitude of $Z_o(s) + Z_g(s)$. Using grid voltage feedforward method can boost the inverter output impedance, praiseworthy. However, this method introduces negative phase angle to the control system which could lead to instability in weak grids [1]. The main idea is introducing a virtual admittance such as $Y_{op}(s)$ in Fig. 6 in order to boost the equivalent output impedance $Z'_o(s)$.

$$Z'_o(s) = \frac{Z_o(s)Z_{op}(s)}{Z_o(s) + Z_{op}(s)} ; \quad Z_{op}(s) = \frac{1}{Y_{op}(s)} \qquad (10)$$

From (10), it can be seen that $Z'_o(s)$ could be increased infinitely if the parallel impedance $Z_{op}(s)$ is set to $-Z_o(s)$.
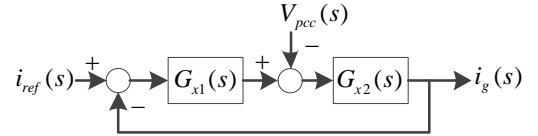
Fig. 4. The equivalent transformation of control block diagram of the grid-connected inverter.
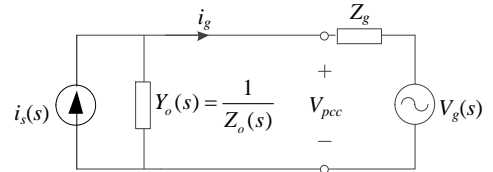
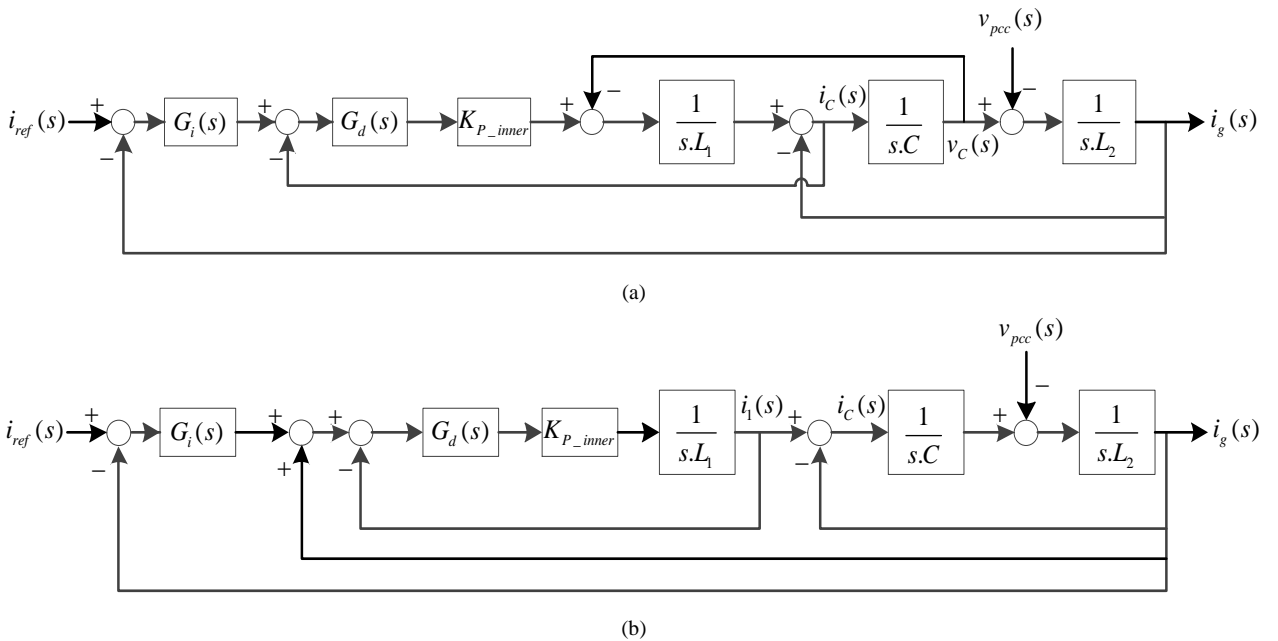Fig. 5. Equivalent circuit of grid-connected inverter.

(a)

(b)

Fig. 3. (a) Block diagram of the dual-loop control strategy based on capacitor current feedback. (b) Simplified block diagram of the aforementioned dual-loop control strategy.

3

Complete analysis about virtual admittance is done in [1]. The control block diagram of grid-connected inverter with virtual admittance is shown in Fig. 7. In this figure, the implementation function of the parallel admittance $G_z(s)$ can be expressed as (11) [1].

$$G_z(s) = \frac{s^2 L_1 C + sCK_{P\_inner}G_d(s) + 1}{K_{P\_inner}} \quad (11)$$

2.3. Proposed Grid Voltage Feedforward Method

As shown in (11), $G_z(s)$ has a second-order derivative element which increases the noise sensitivity. Hence, the implementation function can be closely approximated as

$$G_z(s) \approx G_z'(s) = \frac{sCK_{P\_inner}G_d(s) + 1}{K_{P\_inner}} \quad (12)$$

Using (12), Fig. 7 and signal flow graph (SFG), the shaped output impedance $Z_o'(s)$ can be obtained as

$$
\begin{aligned}
Z_o'(s) &= \frac{v_{pcc}}{-i_g(s)} \\
&= \frac{1 + T(s)}{G_{x2}(s)} \cdot \left[\frac{1}{1 - \frac{Z_C G_d(s) + K_{P\_inner}G_d^2(s)}{Z_{L1} + Z_C + K_{P\_inner}G_d(s)}} \right] \\
&= Z_o(s) \cdot \left[\frac{1}{1 - \frac{Z_C G_d(s) + K_{P\_inner}G_d^2(s)}{Z_{L1} + Z_C + K_{P\_inner}G_d(s)}} \right] \quad (13)
\end{aligned}
$$

The main challenge in implementation of grid voltage feedforward method is that this method introduces negative phase angle to the control system which could lead to instability in weak grids. Typical frequency response of the inverter output impedance $Z_o(s)$ and the shaped output impedance $Z_o'(s)$ are plotted in Fig. 8. The parameters which are used for these plots are related to inverter1 parameters in Table 1 and Set II parameters in Table 2. As shown in Fig. 8, the shaped output impedance $Z_o'(s)$ has higher magnitude than inverter output impedance $Z_o(s)$ which validates the harmonic rejection capability of traditional grid voltage feedforward method. However, a deep phase lag is introduced as shown in phase plot of $Z_o'(s)$. The system will be stable if the phase margin (PM) in the intersection point of $Z_g(s)$ and $Z_o'(s)$ (f_i) to be a possitive value, i.e., PM > 0 [1], [26]. The PM is expressed as

$$\text{PM} = 180° - [\angle Z_g(f_i) - \angle Z_o'(f_i)] \quad (14)$$
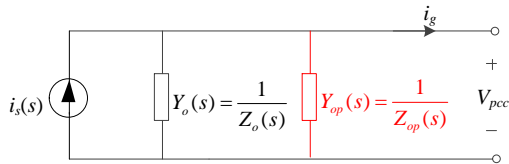

Fig. 6. Equivalent circuit of grid-connected inverter including virtual admittance $Y_{op}(s)$.
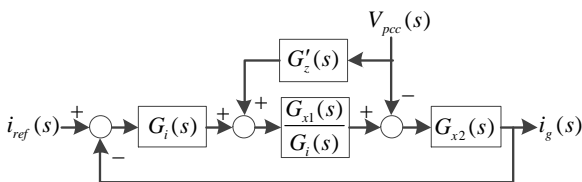

Fig. 7. The equivalent transformation of control block diagram of the grid-connected inverter with grid voltage feedforward method.
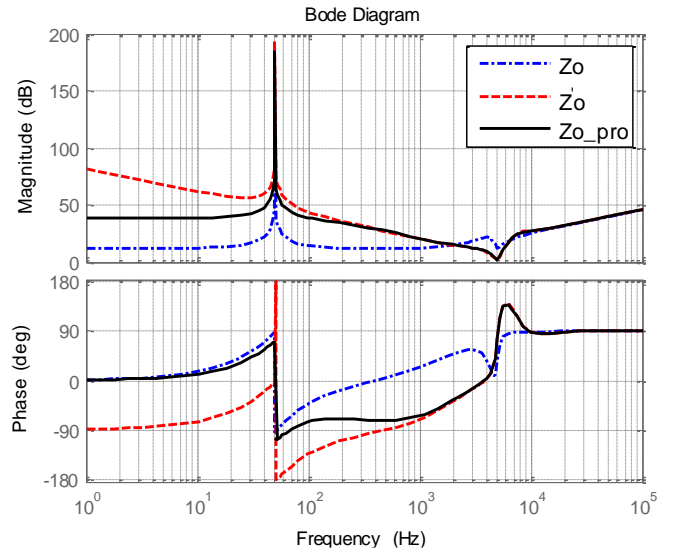

Fig. 8. Frequency response of inverter output impedance Z_o, shaped output impedance Z_o' and proposed output impedance Z_{o_pro}.

Therefore, to improve stability-robustness, it is necessary to boost the phase angle of $Z_o'(s)$ to acquire sufficient PM. In this paper, a simple and improved grid voltage feedforward method is proposed which solves the problem of traditional method.

According to (13) $Z_o'(s)$ is composed of two parts, i.e. $Z_o(s)$ and a fractional part. $Z_o(s)$ is determined by control system and *LCL* filter. Therefore, if $Z_o(s)$ is modified in order to enhance phase angle of $Z_o'(s)$, then the loop gain will change which is not desirable. Besides, increasing the phase angle of $Z_o'(s)$ is limited in this method due to stability constraint. However, the second part of (13) can be used for this purpose because it is introduced due to feedforward path and has not significant effect on main loop gain. Referring (13), the second part of $Z_o'(s)$ is written as

$$Z_{p2}'(s) = \left[\frac{1}{1 - \frac{Z_C G_d(s) + K_{P\_inner}G_d^2(s)}{Z_{L1} + Z_C + K_{P\_inner}G_d(s)}} \right] \quad (15)$$

The frequency response of Z_{p2}' is plotted in Fig. 9. As shown in this figure, it introduces a deep phase lag about -90° in lower frequencies. The main reason for this phase lag is related to fractional part in denominator of (15). The fractional part is given by (16).

$$Z_{p2\_f}'(s) = \frac{Z_C G_d(s) + K_{P\_inner}G_d^2(s)}{Z_{L1} + Z_C + K_{P\_inner}G_d(s)} \quad (16)$$

The frequency response of Z_{p2_f}' is plotted in Fig. 10. As shown in this figure, the magnitude of Z_{p2_f}' is very close to unity in lower frequencies. In fact, it is a bit greater than 1, which is shown in zoomed area. In lower frequencies, G_d can be neglected (e.g. $G_d = 1$) and therefore, Z_{p2_f}' can be written as (17).

$$Z_{p2\_f}'(s) \approx \frac{K_{P\_inner} + Z_C}{K_{P\_inner} + Z_{L1} + Z_C} \quad (17)$$

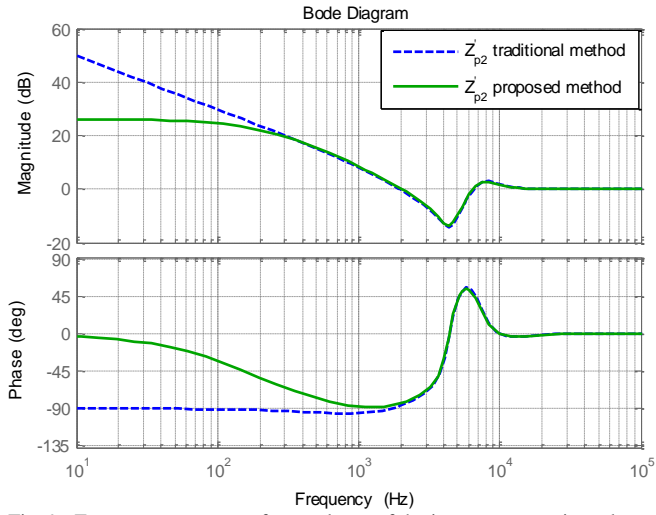In frequency domain, Z_{p2_f}' can be written as

4

Fig. 9. Frequency response of second part of the inverter output impedance (Z'_{p2}): traditional method and proposed method.

$$Z'_{p2\_f}(j\omega) \approx \frac{K_{P\_inner} + \dfrac{1}{j\omega C}}{K_{P\_inner} + j\omega L_1 + \dfrac{1}{j\omega C}}$$

$$= \frac{K_{P\_inner} - \dfrac{j}{\omega C}}{K_{P\_inner} + j(\omega L_1 - \dfrac{1}{\omega C})} \qquad (18)$$

If $\dfrac{1}{\omega C} > \omega L_1$, then the real part of $Z'_{p2\_f}(j\omega)$ will be greater than 1, ($real\{Z'_{p2\_f}(j\omega)\} > 1$). Aforementioned constraint is confirmed at lower frequencies in nearly all cases because the filter capacitor C, has a very small value in comparison with inverter-side inductor L_1, as in our case study. When real part of Z'_{p2_f} is greater than 1 in lower frequencies, Z'_{p2} has a negative real part which causes phase lag. A proportional gain can be used to prevent this phase lag. If a proportional gain that is smaller than 1 inserted in the feedforward path, denominator of (15) will have a positive real part and phase lag will be mitigated. The proportional gain can be selected as

$$G_m \le \frac{1}{|Z'_{p2\_f}(j\omega)|} \qquad (19)$$

It should be noted that the proportional gain G_m should not be selected much smaller than $\dfrac{1}{|Z'_{p2\_f}(j\omega)|}$ since it reduces the magnitude of inverter output impedance in lower frequencies. However, if in a specific case, $|Z'_{p2\_f}(j\omega)|$ to be smaller than 1 in lower frequencies, then there is no need to add any proportional gain. The proportional gains for inverters (G_m) can be calculated using (19). Using parameters in Table 1 and Set II parameters in Table 2 the gains are calculated as $G_{m1} \le 0.988$, $G_{m2} \le 0.956$ and $G_{m3} \le 0.979$ for first, second and third inverters, respectively. Regarding calculated values, the proportional gain is selected $G_m = 0.95$ for all three inverters. The frequency response of proposed Z'_{p2} for inverter1 is also

plotted in Fig. 9. As shown in this figure, the phase lag is mitigated in lower frequencies.

According to aforementioned analysis, the proposed output impedance Z_{o_pro} can be represented as

$$Z_{o\_pro}(s) =$$

$$Z_o(s) \cdot \left[\frac{1}{1 - \dfrac{Z_C G_d(s) + K_{P\_inner} G_d^2(s)}{Z_{L1} + Z_C + K_{P\_inner} G_d(s)} \cdot G_m} \right] \qquad (20)$$

The frequency response of the proposed inverter output impedance Z_{o_pro} is also shown in Fig. 8. It is clearly shown that the phase angle of Z_{o_pro} is boosted in comparison with $Z'_o(s)$, praiseworthy. Indeed, by boosting the phase angle of inverter output impedance, the system stability is guaranteed according to (14). It is the main advantage of the proposed grid voltage feedforward method with respect to traditional one. According to magnitude plot of Fig. 8, the magnitude of Z_{o_pro} is smaller than $Z'_o(s)$ in frequencies below 150 Hz, especially in frequencies below 50 Hz. It is not a big challenge because generally harmonic components in the grid voltage have frequencies higher than 150 Hz (third harmonic). In fact, the proposed method achieves a trade-off between the stability and harmonic rejection capability of grid-connected inverters. With the proposed method, the grid-injected current harmonics caused by grid voltage harmonics can be effectively suppressed while the stability is also guaranteed under weak grid condition. The equivalent block diagram model of the system with proposed grid voltage feedforward method is shown in Fig. 11.
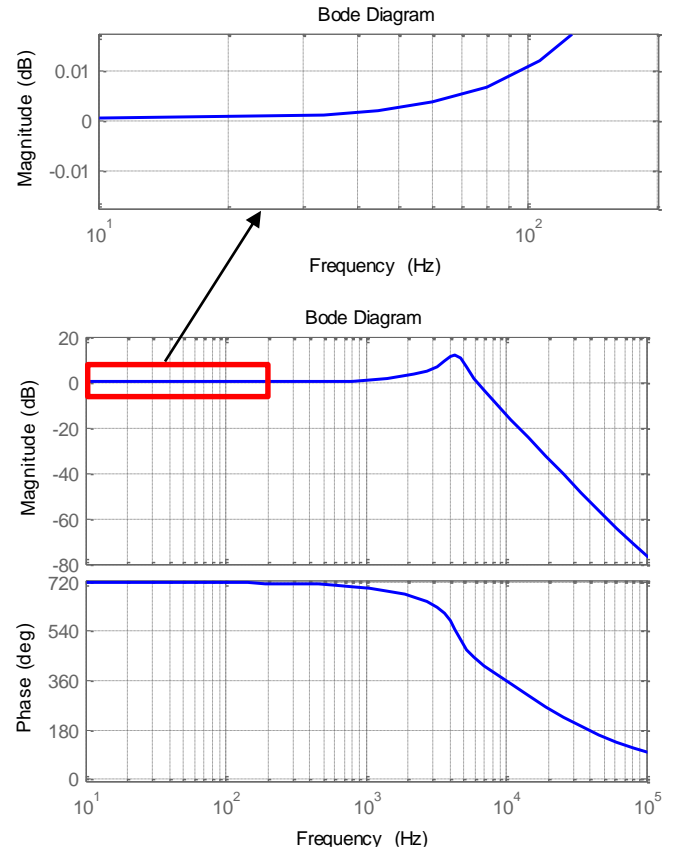

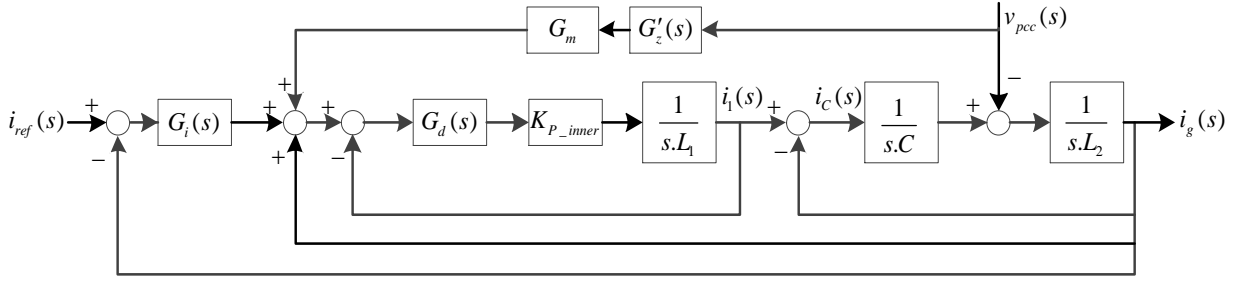Fig. 10. Frequency response of Z'_{p2_f}.

Fig. 11. Block diagram of dual-loop control strategy based on capacitor current feedback with the proposed grid voltage feedforward method.

3. Modeling and Control of Multi-Parallel Grid-Connected Inverters

3.1. System Description

A set of *N*-parallel *LCL*-filtered grid-connected inverters is shown in Fig. 1. The dynamics of these inverters are coupled due to the grid impedance. The equivalent circuit of the *N*-parallel inverters of Fig. 1 is shown in Fig. 12, where Z_{1i}, Z_{2i} and Z_{3i} ($i = 1...N$) are inverter-side inductor impedance, grid-side inductor impedance and capacitor impedance, respectively, all for *i-th* inverter. Moreover, i_{1i}, i_{2i} and i_{3i} are inverter-side current, grid-side current and capacitor current, respectively. The v_{inv-i} is inverter output voltage and i_g is grid-injected current.

3.2. Modeling

Multivariable control loops corresponding to three parallel grid-connected inverters with *LCL* filters that coupled due to the grid impedance in a microgrid are shown in Fig. 13. This is the Multiple Input Multiple Output (MIMO) version of the Single Input Single Output (SISO) control loop of Fig. 11. In this figure, $\bar{G}_i(s)$ is the matrix transfer function that contains the controllers $G_i(s)$; $\bar{G}_d(s)$ is the diagonal matrix transfer function that contains the delay transfer function $G_d(s)$; $\bar{K}_{P\_inner}$ is the matrix transfer function of the inner loop regulators; $\bar{G}(s)$ is the matrix transfer function representing the relation between inverter-side currents (i_{1i} ; $i=1,2,3$) and inverter output voltages (v_{inv-i}; $i=1,2,3$). Due to coupling effect, this matrix transfer function contains diagonal and non-diagonal elements which will be obtained in the next subsection.
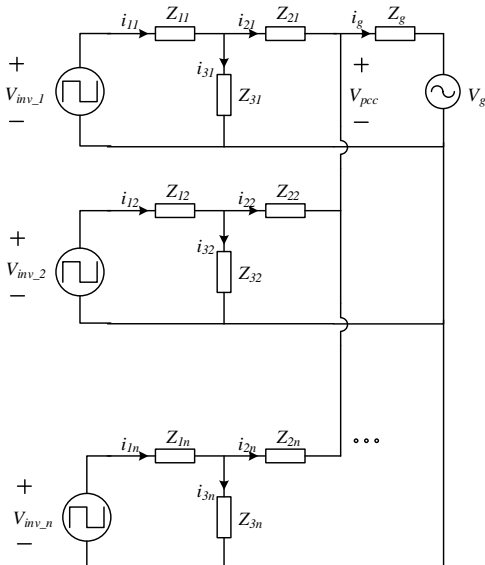

Fig. 12. The equivalent circuit of the *N*-parallel inverters.

3.3. Calculation of the Matrix Transfer Function

Matrix transfer function $\bar{G}(s)$ is represented in (21). This matrix has non-diagonal elements since each inverter output voltage v_{inv_i} influences the output current of other inverters. The elements of the matrix transfer function $\bar{G}(s)$ are calculated using superposition and Thevenin equivalent circuit theorems.

$$\bar{i}_{1n} = \bar{G}(s) \times \bar{v}_{inv}$$

$$\begin{bmatrix} i_{11} \\ i_{12} \\ ... \\ i_{1n} \end{bmatrix} = \begin{bmatrix} G_{11} & G_{12} & ... & G_{1n} \\ G_{21} & G_{22} & ... & G_{2n} \\ ... & ... & ... & ... \\ G_{n1} & G_{n2} & ... & G_{nn} \end{bmatrix} \times \begin{bmatrix} v_{inv1} \\ v_{inv2} \\ ... \\ v_{inv\_n} \end{bmatrix} \quad (21)$$

The diagonal elements are regarded as the transfer functions between the inverter-side current and its own output voltage. Accordingly, for example G_{11} can be calculated if grid voltage and all the inverter output voltages v_{inv_i} are supposed to be zero except v_{inv_1}. For this purpose, the auxiliary circuit of Fig. 14 is derived from Fig. 12. In this circuit, the output current is i_{11} and the only voltage source is v_{inv_1}. Therefore, the diagonal element G_{11}, is directly obtained as follows:

$$G_{11} = \frac{i_{11}}{v_{inv1}} \quad (22)$$

$$= \frac{1}{Z_{11} + \left(Z_g \left\| \left[Z_{23} + \left(Z_{13} \| Z_{33} \right) \right] \right\| \left[Z_{22} + \left(Z_{12} \| Z_{32} \right) \right] + Z_{21} \right) \| Z_{31}}$$

Similarly, other elements of the matrix transfer function $\bar{G}(s)$ are calculated as presented in Appendix.

4. Control System Design

In order to determine the interaction between loops of a MIMO system, relative gain array (RGA) method can be used [27]. The RGA of a non-singular square matrix $\bar{G}(s)$ is defined as

$$\Lambda = \bar{G}(0).\times \bar{G}(0)^{-T} \quad (23)$$

Where $.\times$ denotes element-by-element multiplication and $\bar{G}(0)$ is the matrix $\bar{G}(s)$ in the steady-state condition ($\omega=0$). The RGA is a square matrix which has some unique properties, i.e. the sum of its rows as its columns are equal to 1. If diagonal elements of the RGA matrix be close to unity, the system is diagonally dominant. In other words, interaction of loops in the system is relatively low. Since in described control loops, only matrix transfer function $\bar{G}(s)$ has non-diagonal elements, therefore, the RGA of this matrix should be calculated. By using parameters given in
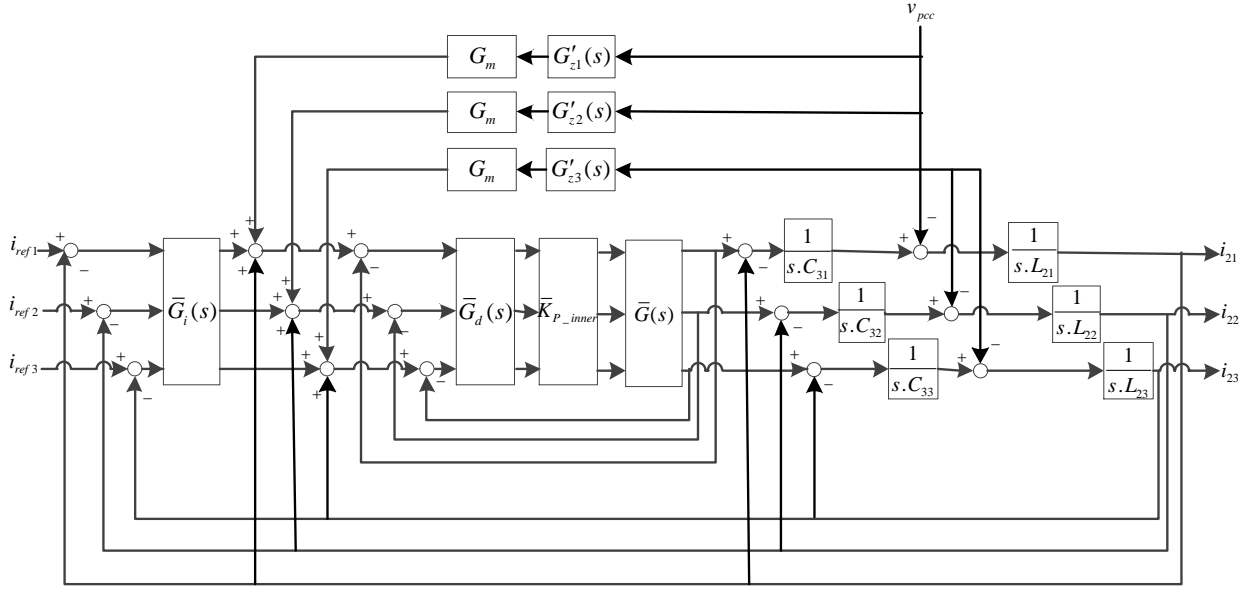
6

Fig. 13. Multivariable control loops for three parallel grid-connected inverters with LCL filters.
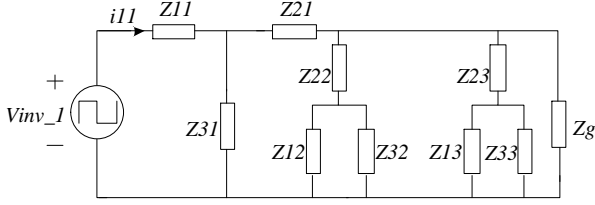

Fig. 14. Auxiliary circuit of the three parallel inverters provided that grid voltage and all inverter voltages v_{inv-i} are zero except v_{inv-1}.

Table 1, the matrix transfer function $\bar{G}(0)$ can be calculated as:

$$\bar{G}(0) = \begin{bmatrix} 1.7757 & -0.3738 & -0.2804 \\ -0.3738 & 2.7103 & -0.4673 \\ -0.2804 & -0.4673 & 2.1495 \end{bmatrix} \quad (24)$$

Therefore, the RGA matrix can be easily calculated as:

$$\Lambda = \bar{G}(0) \cdot \times \bar{G}(0)^{-T}$$
$$= \begin{bmatrix} 1.0654 & -0.0374 & -0.0280 \\ -0.0374 & 1.0841 & -0.0467 \\ -0.0280 & -0.0467 & 1.0748 \end{bmatrix} \quad (25)$$

According to calculated RGA matrix, diagonal elements are close to unity and non-diagonal elements are close to zero. Hence, if cut-off frequency of each main loop designed as high as possible, the interaction of loops can be neglected. It should be noted that with this assumption, the coupling due to the grid impedance remains because any diagonal elements of matrix $\bar{G}(s)$, for example G_{11}, includes the elements of other inverters (Z_{12}, Z_{22}, Z_{13}, Z_{23} and etc.). However, if in another case study, the diagonal elements of RGA matrix be far from unity, the pre-compensator matrix can be used to reduce the interactions [27]. In order to design the inner loop and outer loop controllers, the control system block diagrams of three parallel grid-connected inverters are shown in Fig. 15(a)-(c). In these figures G_{11}, G_{22} and G_{33} are diagonal elements of $\bar{G}(s)$. Also, the PR controller as (26) is used due to its high gain at fundamental frequency.

Table 1
Parameters of the inverters and grid

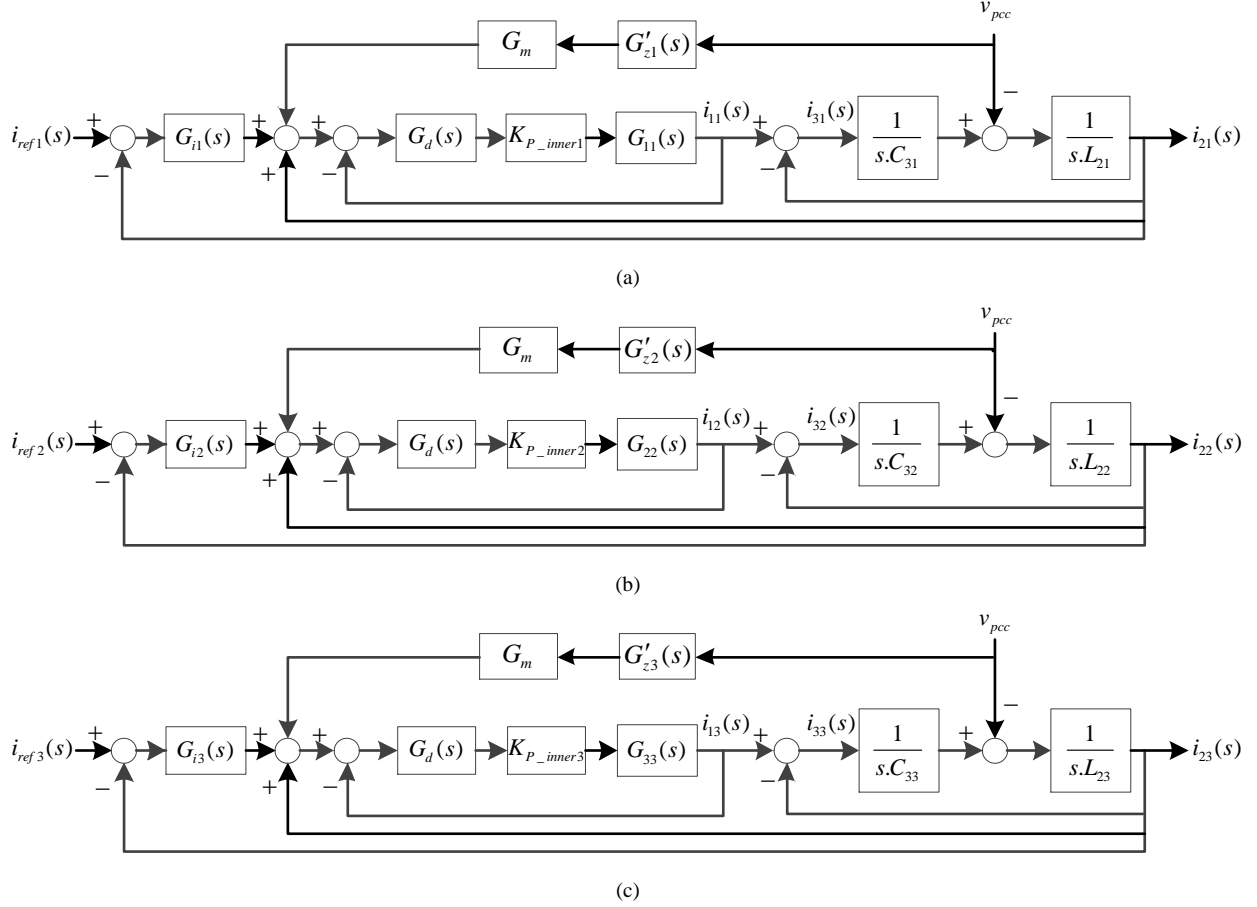| Parameters of the inverter1	
Input DC voltage, V_{dc_1}	360 V
Inverter-side impedance $Z_{11}(R_{11}, L_{11})$	L_{11}=330 µH R_{11}=0.2 Ω
Grid-side impedance $Z_{21}(R_{21}, L_{21})$	L_{21}=330 µH R_{21}=0.3 Ω
Impedance of filter capacitor $Z_{31}(R_{31}, L_{31})$	C_{31}=10 µF R_{31}=0.2 Ω
Sampling frequency	30 kHz
Parameters of the inverter2	
Input DC voltage, V_{dc_2}	360 V
Inverter-side impedance $Z_{12}(R_{12}, L_{12})$	L_{12}=1 mH R_{12}=0.1 Ω
Grid-side impedance $Z_{22}(R_{22}, L_{22})$	L_{22}=1 mH R_{22}=0.2 Ω
Impedance of filter capacitor $Z_{32}(R_{32}, L_{32})$	C_{32}=13 µF R_{32}=0.3 Ω
Sampling frequency	30 kHz
Parameters of the inverter3	
Input DC voltage, V_{dc_3}	360 V
Inverter-side impedance $Z_{13}(R_{13}, L_{13})$	L_{13}=600 µH R_{13}=0.3 Ω
Grid-side impedance $Z_{23}(R_{23}, L_{23})$	L_{23}=200 µH R_{23}=0.1 Ω
Impedance of filter capacitor $Z_{33}(R_{33}, L_{33})$	C_{33}=10 µF R_{33}=0.2 Ω
Sampling frequency	30 kHz
Parameters of the grid	
Grid Voltage, V_g (RMS)	220 V
Fundamental frequency f_0	50 Hz
Grid impedance $Z_g(R_g, L_g)$	L_g=1.3 mH R_g=0 Ω

(a)

(b)

(c)

Fig. 15. Control system block diagram (a) Inverter1. (b) Inverter2. (c) Inverter3.

$$G_i(s) = k_p + \frac{k_r s}{s^2 + \omega_0^2} \qquad (26)$$

where, $\omega_0 = 2 \times \pi \times f_0$ and f_0 is the fundamental frequency.

5. Simulation Results

In this section, a single phase microgrid with three parallel grid-connected inverters with *LCL* filter is simulated using MATLAB/Simulink software. The simulation results are analyzed to validate the theoretical study in previous sections and different aspects of the proposed method are investigated. The key parameters of the inverters and grid are given in Table 1.

5.1. Sinusoidal Grid Voltage Condition

In the first step, to show the necessity of considering the coupling effect in multi-parallel grid-connected inverters, two simulations with and without considering the coupling effect are performed in sinusoidal grid voltage condition. The control parameters of Set I in Table 2 are designed

without considering the coupling effect of three inverters. In other words, the block diagram of Fig. 11 is used for design of controllers of each inverter, individually. The magnitudes of reference injected currents (i_{ref}) of these inverters are 20, 30 and 40A, respectively and the corresponding phase angles are 0°. The bode diagrams of the total equivalent output impedance ($Z_{eq} = Z_{o1} \| Z_{o2} \| Z_{o3}$) and the grid impedance are shown in Fig. 16. Note that, the grid voltage feedforward method is not applied in this step. According to (14), if Z_g and Z_{eq} intersect at f_i, PM must be a positive value to show the system stability [1], i.e.

$$\text{PM} = 180° - [\angle Z_g(f_i) - \angle Z_{eq}(f_i)] \qquad (27)$$

As shown in Fig. 16, the PM has a negative value at intersection point (860 Hz) which shows the connection of three parallel inverters is unstable. In Fig. 17(a)-(c), the simulation results for single grid-connected inverter are shown for each inverter. As shown in these figures,

Table 2

Parameters of the controllers

SET I					
Parameters of the controllers of inverter1		Parameters of the controllers of inverter2		Parameters of the controllers of inverter3	
K_{p_inner}	7.35	K_{p_inner}	37.2	K_{p_inner}	15.2
K_p	0.72	K_p	1.29	K_p	0.65
K_r	350	K_r	233	K_r	281
SET II					
Parameters of the controllers of inverter1		Parameters of the controllers of inverter2		Parameters of the controllers of inverter3	
K_{p_inner}	5.37	K_{p_inner}	10.6	K_{p_inner}	6.24
K_p	0.66	K_p	0.34	K_p	0.60
K_r	318	K_r	66.7	K_r	267

8

all three inverters are stable when they are connected to the grid, individually. Total harmonic distortion (THD) of each inverter injected current is given in Table 3 (case 1). The simulation results for parallel connection of all three inverters to the grid, with previous control parameters, are shown in Fig. 18(a)-(c). As shown in these figures, although the individual connection of each inverter to the grid is stable, parallel connection of inverters to the grid will be unstable which validates the theorical results of Fig. 16. The THD of each inverter injected current when all three inverters are paralleled is also given in Table 3 (case 2). The simulation results show that consideration of coupling effect in multi-parallel grid-connected inverters is necessary.

In the next step, Set II control parameters listed in Table 2 is used for simulation. The controller parameters are designed with consideration of coupling effect as shown in Fig. 15(a)-(c). The bode diagrams of the total equivalent output impedance and the grid impedance are shown in Fig. 19. As shown in this figure, PM has a positive value at the intersection point (700 Hz) which shows that the connection of three parallel inverters is stable.

The injected currents of three inverters are shown in Fig. 20(a)-(c). It can be seen that, despite differences in inverters and their control parameters, injected currents track their reference values. The THD of each inverter injected current when all three inverters are paralleled and with consideration of the coupling effect is also given in Table 3 (case 3). Fig. 20 (d) shows the total grid-injected current which is exactly in phase with the PCC voltage and tracks the sum of reference currents thanks to PR controllers.

The simulation results show that consideration of coupling effect in multi-parallel inverters is necessary and also validate the proposed control system in Fig. 15. Also, the analytical results obtained by impedance-based stability criterion in Fig. 16 and Fig. 19 are validated by simulation results. The negative PM at intersection point leads to system instability as shown in Fig. 18 and on the other hand, positive PM leads to system stablity as shown in Fig. 20.
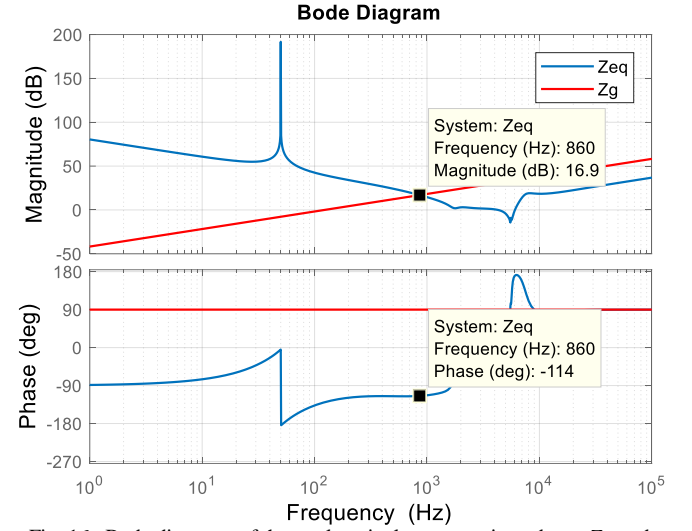

Fig. 16. Bode diagrams of the total equivalent output impedance Z_{eq} and the grid impedance without considering coupling effect.
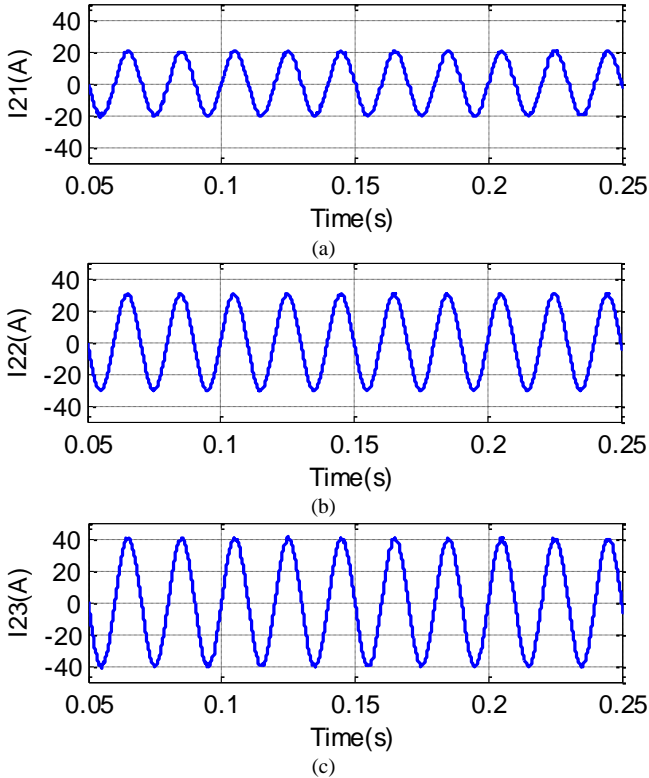

Fig. 17. Simulated waveforms for single grid-connected inverter without considering the coupling effect among inverters in design of controller parameters. (a) Injected current by inverter1 (b) Injected current by inverter2 (c) Injected current by inverter3.
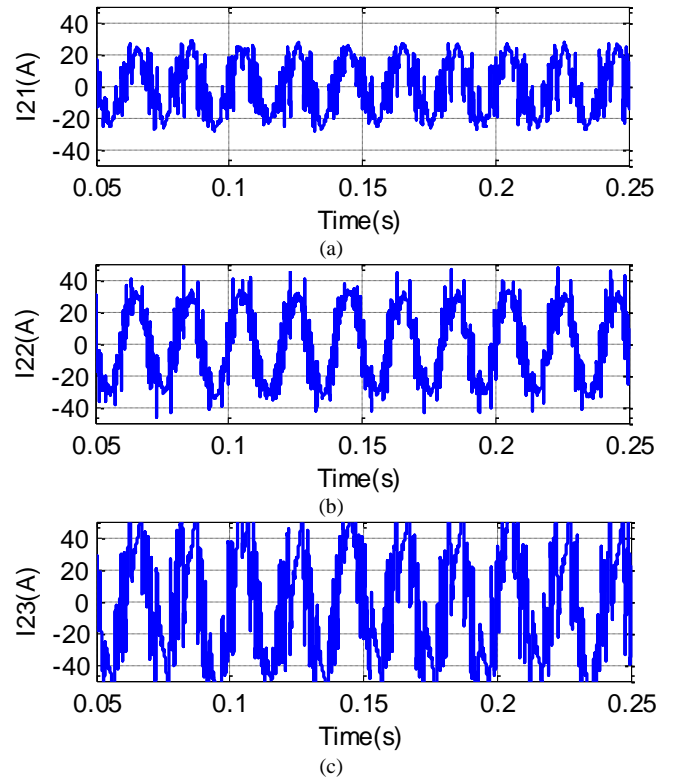

Fig. 18. Simulated waveforms for three parallel grid-connected inverters without consideration of coupling effect among inverters in design of controller parameters. (a) Injected current by inverter1 (b) Injected current by inverter2 (c) Injected current by inverter3.

9

Table 3
The THD of each inverter injected current (sinusoidal grid voltage condition)

Case study	I_{21}	I_{22}	I_{23}
Case1- Single grid-connected inverter without considering the coupling effect in controller design process	3.83%	1.65%	1.48%
Case2- Three grid-connected inverters without considering the coupling effect in controller design process	47.31%	34.16%	42.55%
Case3- Three grid-connected inverters with considering the coupling effect in controller design process	3.46%	0.82%	1.92%

5.2. Non-Sinusoidal Grid Voltage Condition

In order to validate the harmonic rejection capability of the proposed grid voltage feedforward method, two case studies are simulated in non-sinusoidal grid voltage condition: 1) without application of grid voltage feedforward method; 2) with application of proposed grid voltage feedforward method. In this case study, the grid voltage is distorted by third, fifth, seventh, ninth, 11th and 13th harmonics. The magnitudes of harmonic components with respect to the grid fundamental voltage (220 V) are 4%, 3%, 2%, 1.5%, 1% and 0.5%, respectively, and the corresponding phase angles are 0°, 90°, 0°, 270°, 90°, and 105°.

Fig. 21(a)-(d) show the simulation results when the grid voltage feedforward method is not used. The THD of each inverter injected current and also, total grid-injected current are given in Table 4 (Case 1). It can be seen that the grid-injected current of each inverter and also, the total grid-injected current are distorted and power quality is not acceptable at all.

The simulation results for proposed grid voltage feedforward method are shown in Fig. 22(a)-(d). It can be seen that the power quality of injected currents are improved effectively thanks to proposed grid voltage feedforward method. The THD of each inverter injected current and total grid-injected current when the proposed grid voltage feedforward method is used are also given in Table 4 (case 2).
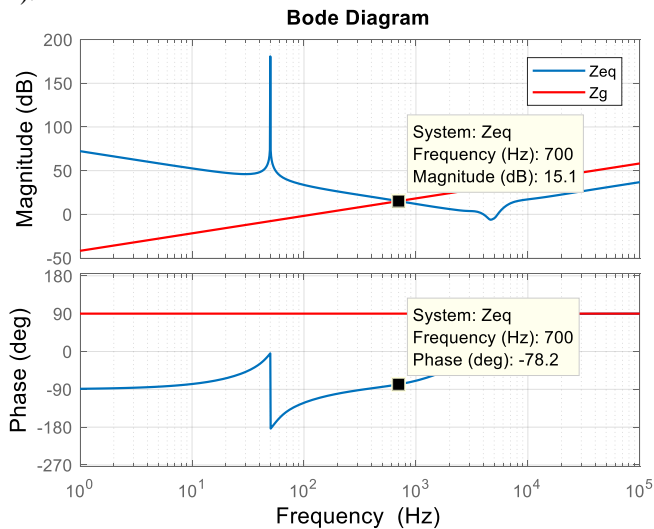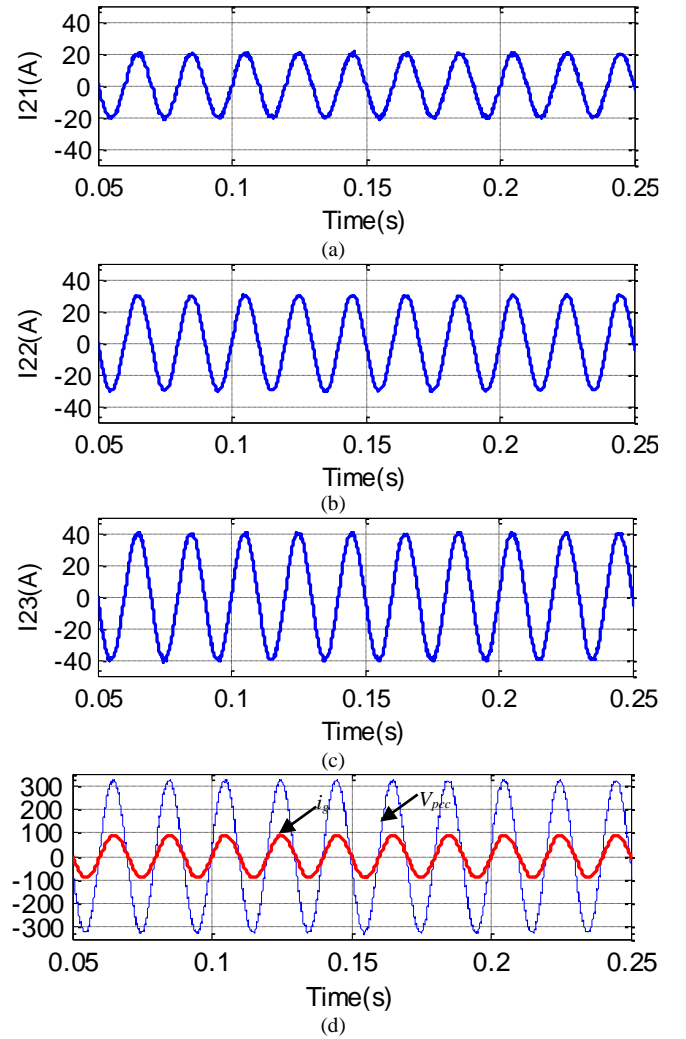

Fig. 20. Simulated waveforms for three parallel grid-connected inverters with consideration of coupling effect among inverters in design of controller parameters. (a) Injected current by inverter1. (b) Injected current by inverter2. (c) Injected current by inverter3. (d) Total grid-injected current (i_g) and PCC voltage (V_{pcc}).

As expected, boosting of inverter output impedance using proposed method has a great impact on quality improvement of grid-injected current and grid voltage harmonic rejection capability. Simulation results validate the capability of the proposed grid voltage feedforward method in non-sinusoidal grid voltage condition which is compatible with analytical results of Fig. 8.

5.3. Non-Sinusoidal Grid Voltage in Weak Grid Condition

In the next step, a comparative study is done, which validates superiority of the proposed grid voltage feedforward method with respect to traditional one in weak grid condition with L_g=6mH. As said earlier, traditional grid voltage feedforward method introduces a deep phase lag which could lead to instability when grid impedance increases. Bode diagrams of the total equivalent output impedance with traditional and proposed method are shown in Fig. 23 with grid inductance equal to L_g=6mH. As shown in Fig. 23, when the traditional method is used, PM has a negative value at intersection point (328 Hz) which shows that the system is unstable. In contrast, when the proposed grid voltage feedforward method is used, the system has a positive PM. The simulation results for traditional grid
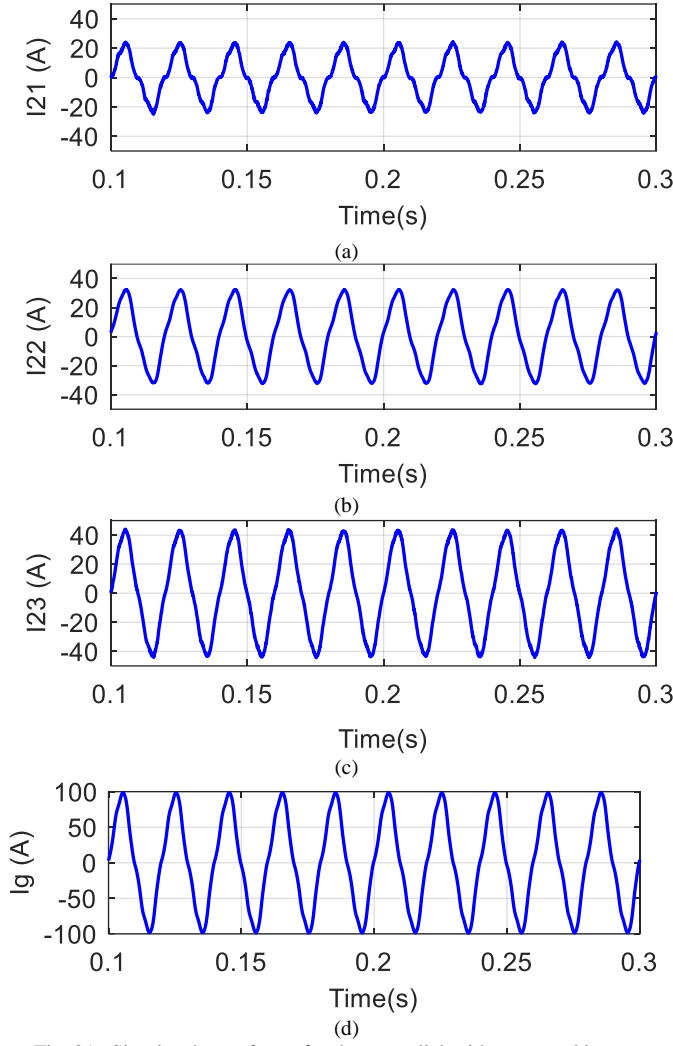

Fig. 19. Bode diagrams of the total equivalent output impedance Z_{eq} and the grid impedance with consideration of coupling effect.

Fig. 21. Simulated waveforms for three parallel grid-connected inverters without grid voltage feedforward. (a) Injected current by inverter1. (b) Injected current by inverter2. (c) Injected current by inverter3. (d) Total grid-injected current (i_g).
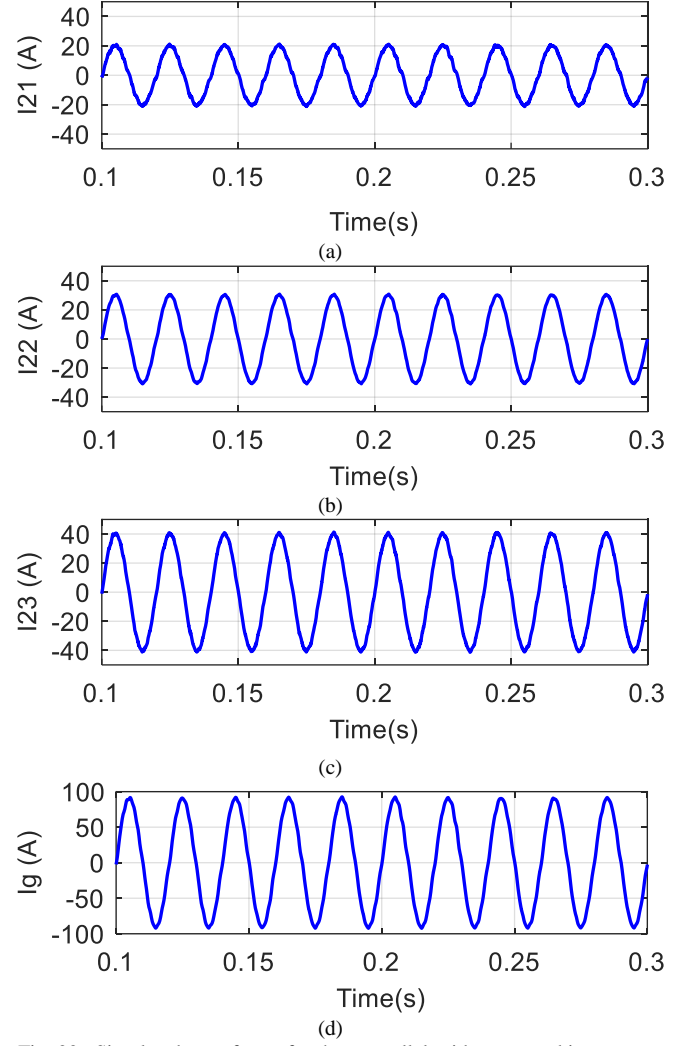

Fig. 22. Simulated waveforms for three parallel grid-connected inverters with grid voltage feedforward. (a) Injected current by inverter1. (b) Injected current by inverter2. (c) Injected current by inverter3. (d) Total grid-injected current (i_g).

voltage feedforward method are shown in Fig. 24(a)-(d). The harmonic components of the grid voltage are same as Section 5.2. i.e. the magnitudes of harmonic components with respect to the grid fundamental voltage (220 V) are 4%, 3%, 2%, 1.5%, 1% and 0.5%, respectively, and the corresponding phase angles are 0°, 90°, 0°, 270°, 90°, and 105°.

It can be seen that the injected currents are distorted seriously, which is compatible with Fig. 23. As stated in Section 2, the traditional grid voltage feedforward method introduces negative phase angle to the control system which could lead to instability in weak grids. The introduced negative phase angle could affect the PM and in case of high grid impedance causes negative PM as shown in Fig. 23. The THD of each inverter injected current and total injected current are shown in Table 5 (Case 1).

Table 4
The THD of each inverter injected current (non-sinusoidal grid voltage condition)

Case study	I_{21}	I_{22}	I_{23}	I_g
Case1- Three grid-connected inverters without using grid voltage feedforward method	19.60%	10.93%	9.44%	11.57%
Case2- Three grid-connected inverters with using proposed grid voltage feedforward method	4.97%	2.85%	2.60%	2.86%

Table 5
The THD of each inverter injected current (non-sinusoidal grid voltage in weak grid condition)

Case study	I_{21}	I_{22}	I_{23}	I_g
Case1- Three grid-connected inverters with using traditional grid voltage feedforward method	14.18%	6.06%	7.50%	8.39%
Case2- Three grid-connected inverters with using proposed grid voltage feedforward method	5.59%	3.77%	4.02%	4.12%

11

Also, the simulation results for proposed grid voltage feedforward method are shown in Fig. 25(a)-(d). The THD of each inverter injected current and total injected current when the proposed grid voltage feedforward method is used are also given in Table 5 (case 2). It should be noted that the quality of injected currents are improved, praiseworthy. As shown in Fig. 23, the phase angle increment using proposed method, causes robust stability of the grid connected system against grid impedance variation. The simulation results in last two case studies show the effectiveness of the proposed grid voltage feedforward method in comparison with traditional one.

5.4. Presence of Non-linear Local Load

The quality of grid-injected current is examined in case of non-linear load connection. In addition to the grid voltage harmonic distortions, another source of current harmonics in a microgrid are nonlinear loads. Hence, to evaluate the effect of non-linear load on the quality of grid-injected current, a thyristor bridge rectifier is connected at the PCC. In this case, the grid voltage is considered sinusoidal and the grid inductance is L_g=1.3mH. The load of the thyristor rectifier is an *RL* load (R=5Ω, L=1 mH).
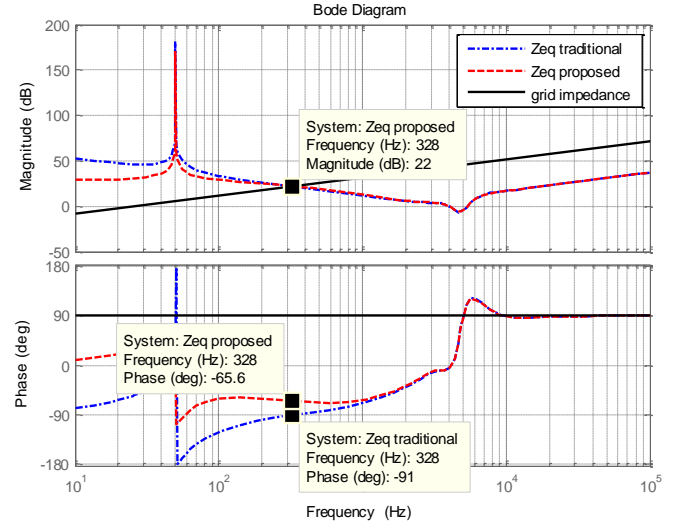
Fig. 23. Bode diagrams of the total equivalent output impedance Z_{eq} with traditional and proposed methods and also the grid impedance.

Fig. 24. Simulated waveforms for three parallel grid-connected inverters with traditional grid voltage feedforward with L_g=6mH. (a) Injected current by inverter1. (b) Injected current by inverter2. (c) Injected current by inverter3. (d) Total injected current (i_g).
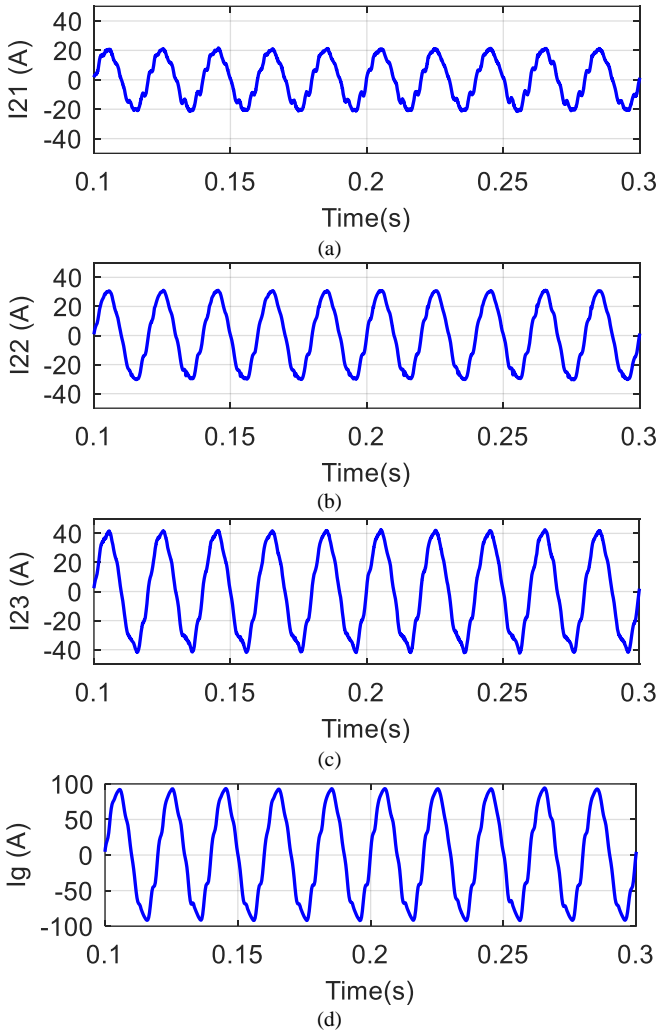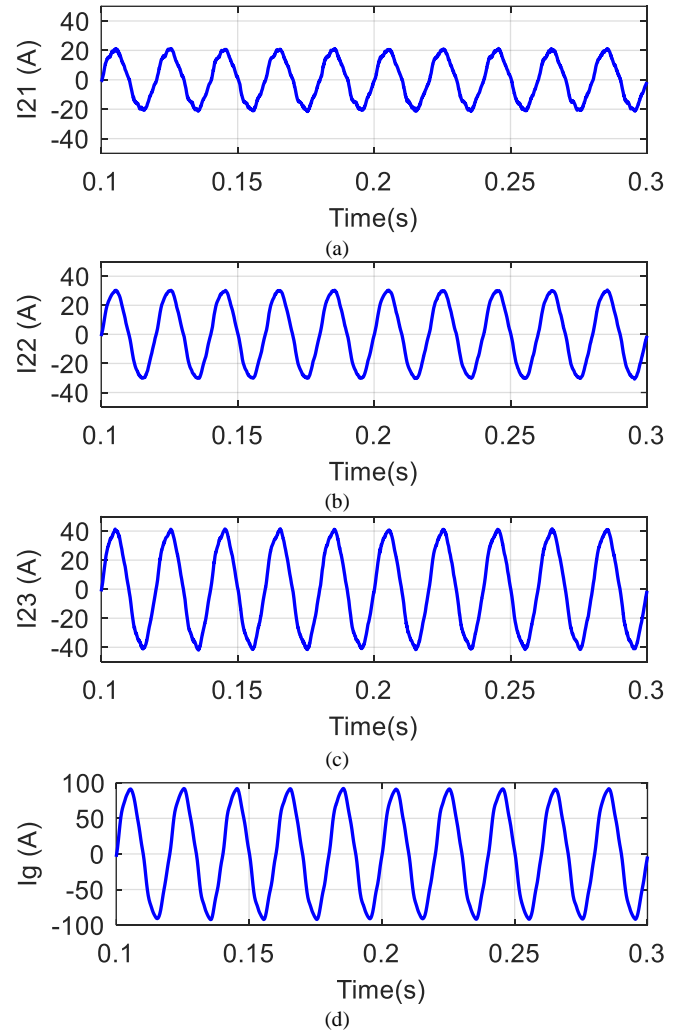
Fig. 25. Simulated waveforms for three parallel grid-connected inverters with proposed grid voltage feedforward with L_g=6mH. (a) Injected current by inverter1. (b) Injected current by inverter2. (c) Injected current by inverter3. (d) Total injected current (i_g).

12

Also, the firing angle of the rectifier is set to 45°. Fig. 26(a) shows the non-linear load current which its harmonic content is extremely high. The grid-injected current without using the grid voltage feedforward method is shown in Fig. 26(b). As shown in this figure, the harmonic distortion is created due to non-linear load connection. The THD value of the grid-injected current is equal to 5.25%. Fig. 26(c) shows the grid-injected current with using the proposed grid voltage feedforward method. As shown in this figure, the harmonic distortion of the grid-injected current is mitigated and the THD value is reduced to 2.04% thanks to proposed grid voltage feedforward method. As shown in this case study, the grid voltage feedforward method can improve the quality of the grid-injected current even in case of non-linear load connection.

5.5. The Impact of Grid Frequency Variation

Finally, the impact of grid frequency variation on the grid-injected current with and without using the proposed grid voltage feedforward method is investigated in this subsection. The previous system contains three parallel grid-connected inverters is simulated considering sinusoidal grid voltage and neglecting grid impedance to demonstrate the impact of grid frequency variation. Magnitudes of the reference currents (i_{ref}) for the invertrs are 20, 30 and 40A, respectively. A step change in grid frequency is occurred at t=0.205s from 50Hz to 49 Hz. Fig. 27(a) shows the total grid-injected current as well as grid voltage when the grid voltage feedforward method is not used. As shown in this figure, the total grid-injected current tracks the sum of reference currents but there is a bit phase shift between the grid voltage and grid-injected current after frequency variation. This leads to a bit reactive power exchange.
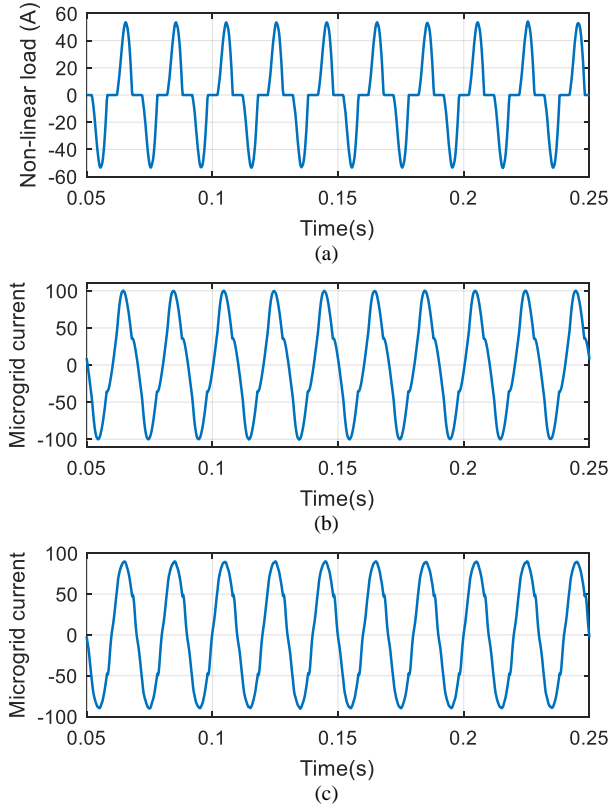

Fig. 26. Simulated waveforms in case of nonlinear load connection. (a) nonlinear load current (b) grid injected current without using the proposed method. (c) Grid injected current with using the proposed method.
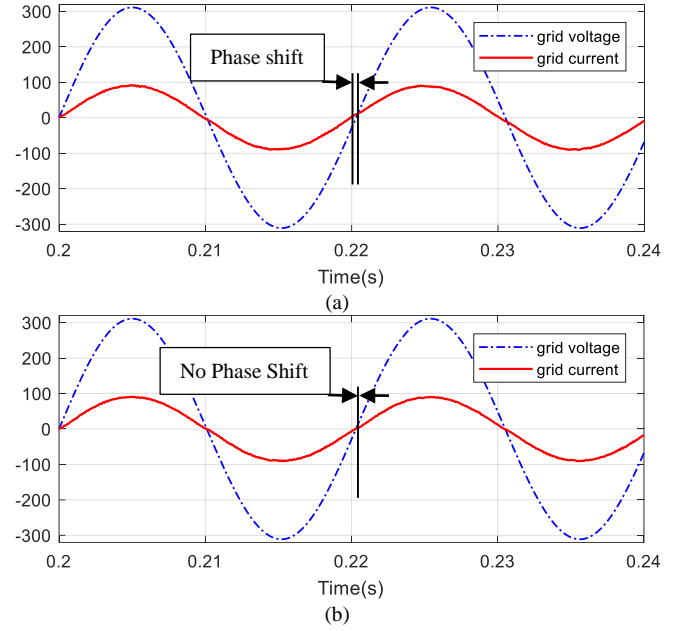

Fig. 27. Simulated waveforms in case of grid frequency variation. (a) Without using grid voltage feedforward method. (c) With using proposed grid voltage feedforward method.

Fig. 27(b) shows the total grid-injected current as well as grid voltage using proposed grid voltage feedforward method. As shown in this figure, the total grid-injected current is exactly in phase with grid voltage and tracks the sum of reference currents in spite of frequency variation. Indeed, by boosting the inverter output impedance the effect of grid voltage is suppressed and the quality of grid-injected current is remained satisfactory even in case of grid frequency variation.

6. Conclusion

In this paper, an improved grid voltage feedforward method is proposed which enhances the grid voltage harmonic rejection capability in multi-parallel grid-connected inverters. By using the proposed method, the negative aspects of the traditional method, that are introducing negative phase angle to the control system and ignoring coupling effect among inverters, are eliminated. The mathematical analysis shows that a proportional gain can be used to prevent phase lag in the control system and improve the system stability in case of grid impedance variation. Also, in the proposed method, the coupling effect among inverters is considered and the system is precisely modeled as a multivariable control system. The presented model facilitates the study of coupling effect among inverters with different characteristics such as *LCL* filters and rated powers. Three parallel grid-connected inverters are considered as a case study. Then, the control system design guidelines are suggested based on multivariable control theory with considering the proposed grid voltage feedforward method and coupling effect among inverters. Numerous simulations were performed which validate the effectiveness of the proposed grid voltage feedforward method in comparison with the traditional one in case of grid impedance variation. Theoretical analysis and simulation results confirm the validity of the model and the necessity to considering the coupling effect among inverters.

Appendix

$$G_{12} = \frac{i_{11}}{v_{inv2}} = \cfrac{1}{\left(1 + \frac{Z_{12}}{Z_{32}} + \frac{Z_{12}}{Z_{22}}\right)\left[-\left(1 + \frac{Z_{22}}{Z_{21}} + \cfrac{Z_{22}}{Z_g \left\|\left[Z_{23} + \left(Z_{13}\|Z_{33}\right)\right]\right.}\right)\left(Z_{11} + Z_{21} + \frac{Z_{11}Z_{21}}{Z_{31}}\right) + \frac{Z_{11}Z_{22}}{Z_{21}}\right] + \frac{Z_{12}}{Z_{22}}\left(Z_{11} + Z_{21} + \frac{Z_{11}Z_{21}}{Z_{31}}\right)}$$

$$G_{13} = \frac{i_{11}}{v_{inv\_3}} = \cfrac{1}{\left(1 + \frac{Z_{13}}{Z_{33}} + \frac{Z_{13}}{Z_{23}}\right)\left[-\left(1 + \frac{Z_{23}}{Z_{21}} + \cfrac{Z_{23}}{Z_g \left\|\left[Z_{22} + \left(Z_{12}\|Z_{32}\right)\right]\right.}\right)\left(Z_{11} + Z_{21} + \frac{Z_{11}Z_{21}}{Z_{31}}\right) + \frac{Z_{11}Z_{23}}{Z_{21}}\right] + \frac{Z_{13}}{Z_{23}}\left(Z_{11} + Z_{21} + \frac{Z_{11}Z_{21}}{Z_{31}}\right)}$$

$$G_{21} = \frac{i_{12}}{v_{inv\_1}} = \cfrac{1}{\left(1 + \frac{Z_{11}}{Z_{31}} + \frac{Z_{11}}{Z_{21}}\right)\left[-\left(1 + \frac{Z_{21}}{Z_{22}} + \cfrac{Z_{21}}{Z_g \left\|\left[Z_{23} + \left(Z_{13}\|Z_{33}\right)\right]\right.}\right)\left(Z_{12} + Z_{22} + \frac{Z_{12}Z_{22}}{Z_{32}}\right) + \frac{Z_{12}Z_{21}}{Z_{22}}\right] + \frac{Z_{11}}{Z_{21}}\left(Z_{12} + Z_{22} + \frac{Z_{11}Z_{22}}{Z_{32}}\right)}$$

$$G_{22} = \frac{i_{12}}{v_{inv\_2}} = \cfrac{1}{Z_{12} + \left(Z_g \left\|\left[Z_{23} + \left(Z_{13}\|Z_{33}\right)\right]\right.\right\|\left[Z_{21} + \left(Z_{11}\|Z_{31}\right)\right] + Z_{22}\right)\|Z_{32}}$$

$$G_{23} = \frac{i_{12}}{v_{inv\_3}} = \cfrac{1}{\left(1 + \frac{Z_{13}}{Z_{33}} + \frac{Z_{13}}{Z_{23}}\right)\left[-\left(1 + \frac{Z_{23}}{Z_{22}} + \cfrac{Z_{23}}{Z_g \left\|\left[Z_{21} + \left(Z_{11}\|Z_{31}\right)\right]\right.}\right)\left(Z_{12} + Z_{22} + \frac{Z_{12}Z_{22}}{Z_{32}}\right) + \frac{Z_{12}Z_{23}}{Z_{22}}\right] + \frac{Z_{13}}{Z_{23}}\left(Z_{12} + Z_{22} + \frac{Z_{12}Z_{22}}{Z_{32}}\right)}$$

$$G_{31} = \frac{i_{13}}{v_{inv\_1}} = \cfrac{1}{\left(1 + \frac{Z_{11}}{Z_{31}} + \frac{Z_{11}}{Z_{21}}\right)\left[-\left(1 + \frac{Z_{21}}{Z_{23}} + \cfrac{Z_{21}}{Z_g \left\|\left[Z_{22} + \left(Z_{12}\|Z_{32}\right)\right]\right.}\right)\left(Z_{13} + Z_{23} + \frac{Z_{13}Z_{23}}{Z_{33}}\right) + \frac{Z_{13}Z_{21}}{Z_{23}}\right] + \frac{Z_{11}}{Z_{21}}\left(Z_{13} + Z_{23} + \frac{Z_{13}Z_{23}}{Z_{33}}\right)}$$

$$G_{32} = \frac{i_{13}}{v_{inv\_2}} = \cfrac{1}{\left(1 + \frac{Z_{12}}{Z_{32}} + \frac{Z_{12}}{Z_{22}}\right)\left[-\left(1 + \frac{Z_{22}}{Z_{23}} + \cfrac{Z_{22}}{Z_g \left\|\left[Z_{21} + \left(Z_{11}\|Z_{31}\right)\right]\right.}\right)\left(Z_{13} + Z_{23} + \frac{Z_{13}Z_{23}}{Z_{33}}\right) + \frac{Z_{13}Z_{22}}{Z_{23}}\right] + \frac{Z_{12}}{Z_{22}}\left(Z_{13} + Z_{23} + \frac{Z_{13}Z_{23}}{Z_{33}}\right)}$$

$$G_{33} = \frac{i_{13}}{v_{inv\_3}} = \cfrac{1}{Z_{13} + \left(Z_g \left\|\left[Z_{21} + \left(Z_{11}\|Z_{31}\right)\right]\right.\right\|\left[Z_{22} + \left(Z_{12}\|Z_{32}\right)\right] + Z_{23}\right)\|Z_{33}}$$

References

[1] D. Yang, X. Ruan, and H. Wu, "Impedance shaping of the grid-connected inverter with *LCL* filter to improve its adaptability to the weak grid condition," *IEEE Trans. Power Electron.,* vol. 29, no. 11, pp. 5795–5805, Nov. 2014.

[2] IEEE Standard for Interconnecting Distributed Resources With Electric Power Systems, IEEE Std. 1547–2003, Jul. 28, 2003.

[3] S. Jayalath and M. Hanif, "Generalized *LCL*-filter design algorithm for grid-connected voltage-source inverter," *IEEE Trans. Ind. Electron.*, vol. 64, no. 3, pp. 1905–1915, Mar. 2017.

[4] E. Kantar and A. M. Hava, "*LCL*-filter design for low-voltage high-power grid-tied voltage-source converter considering various damping methods," in *Proc. IEEE 17th Workshop on Control and Modeling for Power Electronics (COMPEL)*, 2016, pp. 1-8.

[5] W. Li, X. Ruan, D. Pan, and X. Wang, "Full-feedforward schemes of grid voltages for a three-phase *LCL*-type grid-connected inverter," *IEEE Trans. Ind. Electron.*, vol. 60, no. 6, pp. 2237–2250, Jun. 2013.

[6] A. K. Balasubramanian and V. John, "Analysis and design of split-capacitor resistive-inductive passive damping for *LCL* filters in grid-connected inverters," *IET Power Electron.*, vol. 6, no. 9, pp. 1822–1832, Nov. 2013.

[7] W. Yao, Y. Yang, X. Zhang, F. Blaabjerg, and P. C. Loh, "Design and analysis of robust active damping for *LCL* filters using digital notch filters," *IEEE Trans. Power Electron.,* vol. 32, no. 3, pp. 2360–2375, Mar. 2017.

[8] X. Li, X. Wu, Y. Geng, X. Yuan, C. Xia, and X. Zhang, "Wide damping region for *LCL*-type grid-connected inverter with an improved capacitor-current-feedback method," *IEEE Trans. Power Electron.,* vol. 30, no. 9, pp. 5247–5259, Sep. 2015.

[9] F. Wu, J. Ye, X. Luo, Z. Zhang, and Y. Li, "Resonance characteristic analysis and damping control for *LCL*-filter-based voltage source converter during bus transfer," *Electr. Pow. Syst. Res.*, vol. 150, pp. 144–151, Sep. 2017.

[10] X. Wang, X. Ruan, S. Liu, and C. K. Tse, "Full feedforward of grid voltage for grid-connected Inverter with *LCL* filter to suppress current distortion Due to grid voltage harmonics," *IEEE Trans. Power Electron.*, vol. 25, no. 12, pp. 3119-3127, Dec. 2010.

[11] X. Wang, F. Blaabjerg, and P. C. Loh, "Virtual RC damping of *LCL*-filtered voltage source converters with extended selective harmonic compensation," *IEEE Trans. Power Electron.*, vol. 30, no. 9, pp. 4726-4737, Sep. 2015.

[12] Y. Lei, Z. Zhao, F. He, S. Lu, and L. Yin, "An improved virtual resistance damping method for grid-connected inverters with *LCL* filters," in *Proc. IEEE Energy Conversion Congress and Exposition,* 2011, pp. 3816-3822.

[13] D. Pan, X. Ruan, C. Bao, W. Li, and X. Wang, "Capacitor-current-feedback active damping with reduced computation delay for improving robustness of *LCL*-Type grid connected inverter," *IEEE Trans. Power* Electron., vol. 29, no. 7, pp. 3414-3427, Jul. 2014.

[14] S. Y. Park, C. L. Chen, J. S. Lai, and S. R. Moon, "Admittance compensation in current loop control for a grid-tie *LCL* fuel cell inverter," *IEEE Trans. Power Electron.*, vol. 23, no. 4, pp. 1716-1723, Jul. 2008.

[15] Y. Jia, J. Zhao, and X. Fu, "Direct grid current control of *LCL*-filtered grid-connected inverter mitigating grid voltage disturbance," *IEEE Trans. Power Electron.*, vol. 29, no. 3, pp. 1532-1541, Mar. 2014.

[16] J. Xu, S. Xie, and T. Tang, "Active damping-based control for grid-connected *LCL*-filtered inverter with injected grid current feedback only," *IEEE Trans. Ind. Electron.*, vol. 61, no. 9, pp. 4746–4758, Sep. 2014.

[17] M. H. Mahlooji, H. R. Mohammadi, and M. Rahimi,, "Comparison of single loop based control strategies for a grid connected inverter in a photovoltaic system," in *Proc. Power Electronics and Drive Systems Technologies Conference (PEDSTC),* 2016, pp. 390-395.

[18] J. L. Agorreta, M. Borrega, J. López, and L. Marroyo, "Modeling and control of *N*-paralleled grid-connected inverters with *LCL* filter coupled due to grid impedance in PV plants," *IEEE Trans. Power Electron.*, vol. 26, no. 3, pp. 770-785, Mar. 2011.

[19] J. He, Y. W. Li, D. Bosnjak, and B. Harris, "Investigation and active damping of multiple resonances in a parallel-inverter-based microgrid," *IEEE Trans. Power Electron.*, vol. 28, no. 1, pp. 234-246, Jan. 2013.

[20] J. He and Y. W. Li, "Generalized closed-loop control schemes with embedded virtual impedances for voltage source converters with *LC* or *LCL* filters," *IEEE Trans. Power Electron.*, vol. 27, no. 4, pp. 1850–1861, Apr. 2012.

[21] M. Hanif, V. Khadkikar, W. Xiao, and J. L. Kirtley, "Two degrees of freedom active damping technique for *LCL* filter-based grid connected PV systems," *IEEE Trans. Ind. Electron.*, vol. 61, no. 6, pp. 2795–2803, Jun. 2014.

[22] S. Zhang, S. Jiang, X. Lu, B. Ge, and F. Z. Peng, "Resonance issues and damping techniques for grid-connected inverters with long transmission cable," *IEEE Trans. Power Electron.*, vol. 29, no. 1, pp. 110–120, Jan. 2014.

[23] Y. Lei, W. Xu, C. Mu, Z. Zhao, H. Li, and Z. Li, "New hybrid damping strategy for grid-connected photovoltaic inverter with *LCL* filter," *IEEE Trans. Applied Supercond.*, vol. 24, no. 5, pp. 1–8, Oct. 2014.

[24] S. Sing Lee and Y. En Heng, "Optimal VF-PDPC of grid connected inverter under unbalanced and distorted grid voltages," *Electr. Pow. Syst. Res.*, vol. 140, pp. 1–8, Nov. 2016.

[25] A. Akhavan, H. R. Mohammadi, and J. M. Guerrero, "Modeling and design of a multivariable control system for multi-paralleled grid-connected inverters with *LCL* filter," *Int. J Electric Power Energy Syst.*, vol. 94, pp. 354–362, Jan. 2018.

[26] J. Sun, "Impedance-based stability criterion for grid-connected inverters," *IEEE Trans. on Power Electronics,* vol. 26, no.11, pp. 3075 – 3078, Nov. 2011.

[27] A. Khaki-Sedigh and B. Moaveni, Control configuration selection for multivariable plants. Springer, 2009, pp. 13–55.